Role of collisionality and radiative cooling in supersonic plasma jet collisions of different materials

G. W. Collins, IV, J. C. Valenzuela, C. A. Speliotopoulos, N. Aybar, F. Conti, and F. N. Beg
Center for Energy Research, University of California at San Diego, San Diego, California 92093, USA

P. Tzeferacos and B. Khiar
Department of Astronomy and Astrophysics, University of Chicago, 5640 S. Ellis Ave, Chicago, Illinois 60637, USA

A. F. A. Bott and G. Gregori
Department of Physics, University of Oxford, Parks Road, Oxford OX1 3PU, United Kingdom

(Received 21 April 2019; revised manuscript received 5 December 2019; accepted 14 January 2020; published 14 February 2020; corrected 26 October 2020)

Currently there is considerable interest in creating scalable laboratory plasmas to study the mechanisms behind the formation and evolution of astrophysical phenomena such as Herbig-Haro objects and supernova remnants. Laboratory-scaled experiments can provide a well diagnosed and repeatable supplement to direct observations of these extraterrestrial objects if they meet similarity criteria demonstrating that the same physics govern both systems. Here, we present a study on the role of collision and cooling rates on shock formation using colliding jets from opposed conical wire arrays on a compact pulsed-power driver. These diverse conditions were achieved by changing the wire material feeding the jets, since the ion-ion mean free path ($\lambda_{\text{mfp-ii}}$) and radiative cooling rates (P_{rad}) increase with atomic number. Low Z carbon flows produced smooth, temporally stable shocks. Weakly collisional, moderately cooled aluminum flows produced strong shocks that developed signs of thermal condensation instabilities and turbulence. Weakly collisional, strongly cooled copper flows collided to form thin shocks that developed inconsistently and fragmented. Effectively collisionless, strongly cooled tungsten flows interpenetrated, producing long axial density perturbations.

DOI: 10.1103/PhysRevE.101.023205

I. INTRODUCTION

Studying the shocks formed when supersonic astrophysical plasma flows interact with their surroundings, such as Herbig Haro (HH) objects [1,2] and supernova remnants (SNRs) [3,4], can help answer outstanding questions on topics such as stellar formation [5] and cosmic ray generation [6]. The distances and vast scales of these astrophysical objects make studying them directly difficult. Fortunately, repeatable laboratory-scale experiments accompanied by suites of diagnostics can complement direct observations and measurements provided that they meet certain similarity criteria demonstrating that both systems are governed by the same physics [7,8]. Two parameters key to establishing similarity are the collision and cooling rates.

Observations and simulations show that some of the substantial surface features HH objects develop are due to cooling processes such as the thermal condensation instability [9,10]. This instability, which describes the globular formations in galaxies and nebulae not attributable to gravity, is formed when the material-specific plasma cooling function ($\Lambda_c = P_{\text{rad}}/(n_i n_e)$, where n_i is the ion density, n_e is the electron density, and P_{rad} is the radiative cooling rate) increases with decreasing temperature [11,12].

Supernova remnants self-generate electromagnetic fields through collisionless mechanisms such as the Weibel instability. This instability only occurs when the strong anisotropy of interpenetrating flows creates a Lorentz force that can act on spontaneous magnetic perturbations [13–15].

With such diverse conditions required to generate the defining characteristics of these shocks, experiments are generally tailored to specifically reproduce certain collision or cooling rates. To date, the bulk of these experiments utilize the largest laser and current-driving facilities available, largely due to their ability to create high-temperature, high Mach number flows [16–19]. For example, the mega-ampere pulsed power generator MAGPIE was used to perform experiments on colliding jets and produce bow shocks that scaled to HH objects; in the experiment, cooling instabilities were suggested to play an important role in the shock fragmentation [16] as is observed in the astrophysical case. High-power lasers can create collisionless plasmas by irradiating plastic discs to generate flow velocities ~10 times those produced in the pulsed power experiments (10^8 cm/s in laser experiments vs 10^7 cm/s in pulsed power experiments). Experiments on the kilojoule class Omega laser produced Weibel instabilities, recreating the complex self-generated electromagnetic fields seen in SNRs [17,18]. These fields are believed to mediate shocks that are responsible for accelerating cosmic rays. Recently, at the National Ignition laser Facility (~2 MJ), the transition from collisional to collisionless plasma regimes was demonstrated by changing the separation of the plastic disk targets [19].

The results presented in this paper demonstrate that a simple setup can provide access to a wide range of collisionalities and cooling parameters required for astrophysical scaling using a university-scale, pulsed-power driver at the University of California, San Diego.

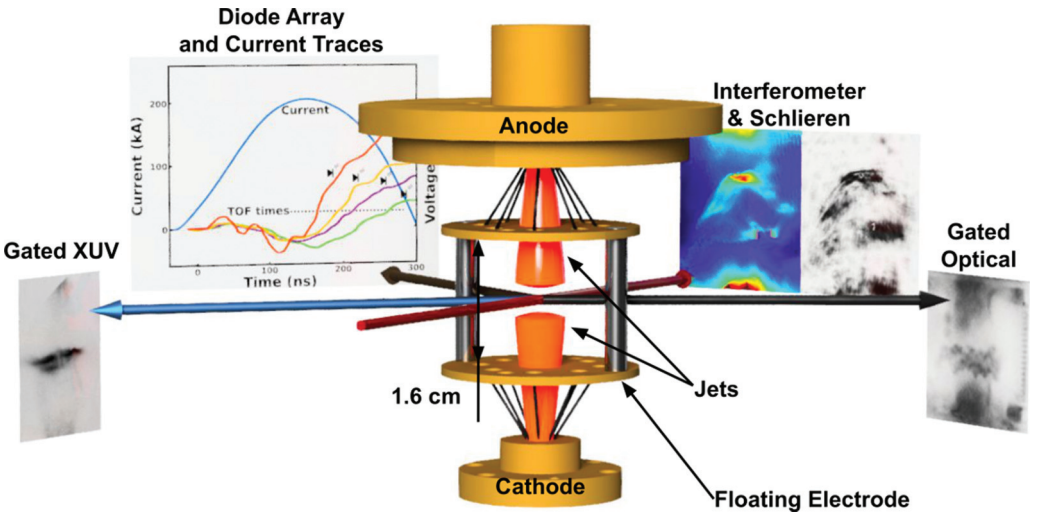

FIG. 1. A three-dimensional scaled drawing of the array setup that is loaded into the chamber is provided along with the approximate diagnostic paths and samples of their results. A typical current profile from GenASIS is provided along with the voltage traces for the diode array diagnostic. The space between the floating electrodes measures 1.6 cm, while the height of each conical array is 0.8 cm.

II. EXPERIMENTAL SETUP AND DIAGNOSTICS

The experiments detailed here collided two counter-propagating plasma flows from opposed conical wire arrays opening towards each other [20–22] on the 200 kA, 150 ns rise-time GenASIS driver [23]. A diagram of the setup is given in Fig. 1, showing the two conical wire arrays (eight wires each) separated by a central support that was isolated from the anode and cathode of GenASIS by being suspended by the top conical array and anchored gravitationally by the bottom array. This central support, dubbed the 'floating electrode', allowed jets to propagate through 0.5 cm apertures at either end into a 1.6 cm interaction region free of non-jet plasma from the arrays.

Changing the cooling and collision rates of the jets simply involved changing the wire material in the conical arrays that supplied the jets, since the cooling function, Λ_c, scales with atomic number [24], and the ion mean free path, $\lambda_{\text{mfp-ii}}$, scales with the atomic mass (A) to the second power [detailed later in Eq. (1)]. While other parameters including ionization level (Z^*), ion density (n_i), electron temperature (T_e), and jet velocity (u_{jet}) also affect the cooling and collision rates of the plasma, changing the material both directly and indirectly played a larger role in changing the two rates in question. The materials used here were 200 μm carbon, 25 μm aluminum, 25 μm copper, and 10 μm tungsten. Material purity of the Al, Cu, and W wires (purchased from California Fine Wire Co., Goodfellow and Goodfellow, respectively) was $\geqslant$99% while the C 'wires' were 0.02 cm Ain Stein 2B pencil lead. The wires sizes were chosen to be overmassed (no chance of early pinching or implosion), and strong enough to suspend the floating electrode while maintaining order-of-magnitude comparable mass-per-until lengths (except C). While previous work using a similar setup on GenASIS produced bow-shocks using Al and Cu flows that were scalable to Herbig-Haro objects (see Ref. [22]), the aforementioned array design improvement (using the isolated floating electrode, while the previous work mounted the central support electrode with an insulator to the anode) produced symmetrical jet interactions and enabled the use of more resistive wire materials including carbon and tungsten which dramatically increased the accessible range of collisionalities and cooling rates.

These experiments were probed with a 200 mJ, 1064 nm, 5 ns pulse width Nd-YAG laser configured to a simultaneous four-frame Mach-Zehnder interferometer and schlieren setup for a total of eight images. The four frames were created using a polarizing beam splitter on 45° polarized light to create two orthogonally polarized beams. One was delayed 15 ns and the two were recombined and then split 50/50, with one pair proceeding through the target chamber, and the other pair delayed another 30 ns (making 0, 15, 30, and 45 ns relative frame delays) before then passing through the target. The beams in each pair overlapped to such a degree that a single schlieren stop could be used to block both, while the two pairs were separated geometrically so they could be 'picked off' with mirrors or beam splitters. The images for the laser diagnostics were captured using Canon DSLR cameras with the IR filter removed from in front of the CCDs. A narrow (3 nm) laser-line filter was mounted on each camera so that their shutters could be left open for a 5 s exposure (during which time GenASIS was triggered) without any significant self-emission or laboratory light reaching the CCDs. The spatial resolution for this setup measured $\sim$50 μm. The interferometer setup provided areal electron density information which was processed using Abel inversions (when there was appropriate symmetry) to obtain electron density. To obtain quantitative structural information from the schlieren images we performed two-dimensional fast Fourier transforms (2D FFTs) and produced Power Spectral Density (PSD) plots. The spherical schlieren stops measured 0.075 cm, which along with the collection optic, yielded a window of observable densities between $\sim 7\times10^{17}$–2×10^{19} e^-/cm^3.

A single-frame gated optical camera (2.6 ns gate width, $\sim$200 μm resolution) and a four-frame gated XUV camera (10 ns gate width, $\sim$190 μm resolution, and a lower photon energy cutoff of $\sim$25 eV) accompanied the laser probing.

TABLE I. Tabulation of critical measured and calculated parameters from single-jet experiments.

Element	u_{jet} (10^5 cm/s)	$\mathcal{M}$	Avg. n_e (10^{17} cm^{-3})	T_e (eV)	Z^*	$\lambda_{mfp\text{-}ii}$ (cm)
C	74 ± 7	3.8 ± 0.9	1.4 ± 0.4	8 ± 1	3.8 ± 0.5	0.12 (0.07–0.24)
Al	99 ± 13	6.8 ± 1.0	1.3 ± 0.3	12 ± 2	3.4 ± 0.6	2.4 (1.1–5.9)
Cu	110 ± 40	5.4 ± 1.7	1.0 ± 0.2	26 ± 6	7.4 ± 1.8	3.2 (0.2–48.0)
W	164 ± 65	>10	0.9 ± 0.3	$\leqslant$10–20	~8–9	63 (2–2300)

A vertical diode array consisting of a biconvex lens that magnified the jet image 3.1X onto optically sensitive Si diodes outside the vacuum chamber measured light from the jets to determine the propagation velocity of the leading edge of said jets. The lines of sight and data samples from each diagnostic are shown around the illustration of the array setup in Fig. 1.

III. DETERMINATION OF JET PARAMETERS

Neither key parameter of interest (the ion-ion mean free path, $\lambda_{mfp\text{-}ii}$, or the radiative cooling rate, P_{rad} in erg cm^{-3} s^{-1}) can be measured directly with the diagnostics available, so they must be calculated from the three experimentally measured quantities: areal electron density, jet velocity (u_{jet}), and the Mach number ($\mathcal{M}$). To determine these parameters, a large number of single-jet shots were done prior to the colliding jet experiments. For these single jet shots, one of the ends of the floating electrode was removed and the two posts were replaced with longer ones mounting the remaining plate to the anode or cathode. This kept the opening angle of the jet, the aperture in the floating electrode, and the relative position to the current carrying posts the same as in the colliding jet setup. Single jets propagating in both directions were tested.

To obtain values for the electron density, n_e, 2D areal electron density maps of the interferograms were created of the single jet shots using the software IDEA [25]. An Abel inversion using a Fourier method [26] was run on the data to obtain the density profile. The Mach number, $\mathcal{M}$ was determined via $1/\arctan(\alpha)$, where α is the opening angle of the jet from vertical. To determine α, the areal electron density full width half-maximum of the jet (from the 2D areal electron density maps) at each vertical pixel along the axis was taken and a line was fit to these points, where the slope of the line corresponded to α and thus $\mathcal{M}$. The quotient of u_{jet} (measured with the diode array) and $\mathcal{M}$ gave the sound speed, c_s, which in turn provided Z^*T_e (ionization level and electron temperature, respectively). The experimental T_e and Z^* were estimated by running the atomic codes PrismSPECT (for C, Al, and Cu) and FLYCHK [27] (for W) with the measured n_e to find the best match between measured and calculated Z^*T_e. This measurement of $\mathcal{M}$ and the subsequently derived parameters is a derivation of the methods used in Refs. [21,28].

Values of the key measurements and calculated parameters from the single jet shots are provided in Table I. Measurements of mean n_e decreased with atomic number, ranging from 1.4×10^{17} cm^{-3} for C to 0.9×10^{17} cm^{-3} for W. Peak values centered around 2×10^{17} cm^{-3} for all materials. Electron temperatures calculated for C, Al, and Cu were 8, 12, and 26 eV, respectively, with 15–25% uncertainty. The tungsten jets did not expand. Because of this the temperature of the W flows was roughly estimated as the point where the energy losses due to radiative cooling (in erg/cm^3) approached between 5 and 50% of the thermal energy (in erg/cm^3) over a 50–100 ns window, which is the time it takes a W jet to propagate through the interaction region. With the measured parameters, this approximate balance occurs around 10–20 eV. The determined values for Z^* are also given in Table I.

Velocities measured with the diode array showed a general increase with atomic mass matching previous studies [29], ranging from 7.4×10^6 cm/s for C to 1.64×10^7 cm/s for W. Diagnostic uncertainty and shot-to-shot variability ranged between ~10–40%. No difference in u_{jet} was measured within the sensitivity limits of the diode array diagnostic between jets propagating up or down.

With the required parameters determined, we can now calculate $\lambda_{mfp\text{-}ii}$ for the counter-propagating flows from equation 5a in Rambo *et al.* [30]. In the event that the flow velocity is more than a few times greater than the thermal velocity ($\mathcal{M} \geqslant$ 3–4), $\lambda_{mfp\text{-}ii}$ simplifies to

$$\lambda_{mfp\text{-}ii} \approx 1.67\times10^{-11}\frac{u_{jet}^4 A^2}{Z^{*4}\ln\Lambda\ n_i}, \tag{1}$$

where $\ln\Lambda$ is the Coulomb logarithm, and $n_i = n_e/Z^*$ is the ion density. All quantities here are in cgs units unless otherwise mentioned. Given the u_{jet}^4 dependence in $\lambda_{mfp\text{-}ii}$, the wide range of measured velocities introduces large uncertainties in the determination of collisionality. Values for $\lambda_{mfp\text{-}ii}$ given in Table I include the average value using all of the determined quantities, and between parentheses a range from the minimum to maximum values compatible with the error bars (where the minimum $\lambda_{mfp\text{-}ii}$ was calculated using the lowest velocity and the highest n_i and Z^*, etc.).

Only collisions between counter-streaming ions have been discussed up to this point. Collisions of ions with electrons of the opposing jet are thought to play various roles in the dynamics of interpenetrating flows such as producing an electron 'drag' on the ions [30–32], and calculations show that the *i-e* mean free path ($\lambda_{mfp\text{-}ie}$) is smaller than the $\lambda_{mfp\text{-}ii}$ by an order of magnitude or more. In the cases of Al and Cu, *i-e* collisions likely play a dynamic role in the interactions between jets. However, given the mass of W ions (the momentum lost by an ion in *i-e* compared to *i-i* collisions scales with $\sim m_e/m_i$), and the relatively long $\lambda_{mfp\text{-}ie}$ (~0.8 cm via Eq. 2 in Ref. [31], and $\gg$1 cm via Eq. 5a in Ref. [30]), the role of *i-e* collisions is assumed negligible here over relevant time and spatial scales. Therefore, collisions between the counter-streaming ions are judged to be the key parameter in defining the collisionality of the W jets here.

P_{rad} was calculated from the tables provided by FLYCHK and PrismSPECT. From these we expect the radiative power

TABLE II. Preliminary tabulation of key dimensionless parameters of the four materials tested here, as well as for HH objects and SNRs.

Regime	$\mathcal{M}$	$\delta_{\rm loc}$	Reynolds # (Re)	Peclet # (Pe)	Cooling parameter χ_c
C	4	10^{-4}	10^5	10–100	10
Al	7	10^{-3}	10^5	10	0.1–1
Cu	5	10^{-3}	10^5	10	0.1–1
W	>10	10^{-3}	10^6	20	0.1–1
HH Objects	5–30	10^{-9}	10^{10}	10^8	0.01–1
SNRs	10–100	10^{-9}	10^{11}	10^9	0.1–1

of the jets to rise by orders of magnitude from C to Al, Cu, and W. Radiation effects become dynamically significant when the cooling timescale $\tau_c \propto T_e/(n_i\,\Lambda_c)$ of the plasma is similar to or smaller than the hydrodynamic timescale $\tau_{\rm hydro} \approx r_{\rm jet}/\mathbf{u}_{\rm jet}$ (where $r_{\rm jet}$ is the jet radius) [7]. Here, $\tau_{\rm hydro}$ ranges from ~30 ns for W to ~60 ns for C, while estimates of τ_c are of the order of 10 ns for W, Cu, and Al interactions, and hundreds of nanoseconds for C.

A. Dimensionless comparison to astrophysical entities

As mentioned in the opening paragraph, the primary motivation behind these experiments is to develop and benchmark a platform for laboratory astrophysics. Before delving into the colliding jet results, we will quickly demonstrate the scalability of the results presented here. Cursory calculations of a few key dimensionless scaling parameters for the different jets tested here as well as for HH objects and SNRs are included in Table II. The parameters presented were calculated using equations primarily from Refs. [7,8]. Evolutionary similarity is established by $\mathcal{M}$: two systems with similar $\mathcal{M}$ and initial geometry should evolve comparably. This was displayed in Table I, and is given again due to its relevance here. To compare the individual flows (not the two colliding) using the fluid equations of motion, the particles must be localized, given by $\delta_{\rm loc} \ll 1$. This is given by the ratio of the mean free path (ion-ion here) and the characteristic scale length, and is a plasma quantity comparable to the Knudsen number (Kn) in fluid dynamics. The governing fluid equations can be further simplified if viscosity and thermal conduction can be neglected, which occurs when the Reynolds number (Re) and Peclet number (Pe) $\gg 1$. As mentioned earlier, the significance of radiative cooling in a system is given by $\chi_c = \tau_c/\tau_{\rm hydro}$, where a radiatively cooled system has $\chi_c < 1$. We find that radiative cooling should play an important roll in Al, Cu, and W flow interactions, but not in those involving C flows.

In all the cases tabulated, the particles are localized and viscosity and thermal conduction can be neglected. Al and Cu jets scale reasonably well to HH objects, where the $\mathcal{M}$'s are similar and radiative cooling is important. The high $\mathcal{M}$ of the W flows makes them a better match to SNRs. C jets could be used to study aspects of HH objects though the lack of cooling limits this.

IV. COLLIDING JET RESULTS AND DISCUSSION

From our calculations of individual jet parameters, we make a handful of assumptions about the colliding-jet experiments for each material. Carbon interactions are collisional or weakly collisional with no significant effects due to radiative cooling. Aluminum and copper interactions are weakly collisional and radiative cooling effects should be dynamically significant. W flow interactions are effectively collisionless.

Figure 2 shows the effect of decreasing collisionality and increasing cooling with atomic mass via early time gated XUV images from counterpropagating jet experiments of typical C (a,b), Cu (c,d), and W (e,f) interactions. The times given are with respect to the initial signs of shock formation or

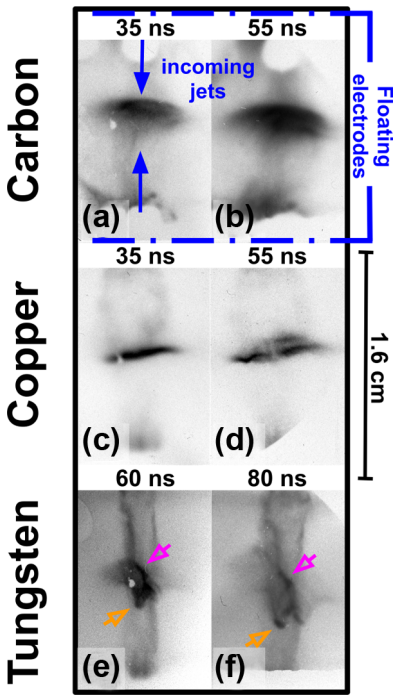

FIG. 2. The relative effects of radiative cooling and collisionality are shown in the early-time XUV images of C (a), (b), Cu (c), (d), and W (e), (f). At this early stage, the decreasing collisionality with increasing atomic mass is clear as C and Cu form shocks while W jets interpenetrate. The thinness of the Cu shock relative to the C shock is characteristic of strong radiative cooling. Denser structures moving apart from the initial interaction region of the W jets are labeled with arrows in (e) and (f). Times relative to shock formation are given at the top of each frame. The positions of the floating electrodes and the locations and directions of the jets are labeled on frames (a) and (b). A scale is given to the right of frame (d). Both frames from each material are from the same shot.

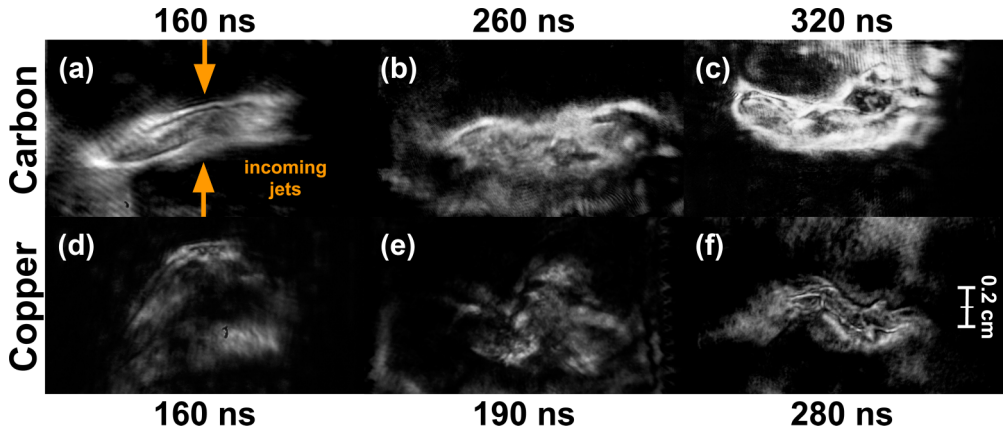

FIG. 3. Schlieren time sequences of colliding C-C and Cu-Cu jet shots. Frames (a)–(c) show the similarity in shape and size of three different C shocks at different times long after formation. Even asymmetry in the initial jets resulting in imperfectly centered shocks did not significantly alter the structure of the shocks. The variability of Cu shocks can be seen in frames (d)–(f), which show three different Cu shocks over time. Times relative to initial jet interaction are shown near each frame. A 0.2 cm scale is given for reference in frame (f), and the direction and approximate location of the jets is given in frame (a).

interaction. At first glance, the effect of decreasing collisions seems clear: the collisional or weakly collisional C and Cu jets form strong shocks, while initial W jet interactions interpenetrate, forming transient density increases [two of which are marked by arrows in Figs. 2(e) and 2(f)] that stream away and develop into predominantly axial perturbations. The thinness of the Cu shock compared to the C shock is characteristic of strong radiative cooling. Additional effects of collisionality and the more subtle roles of cooling will be discussed on a material by material basis.

High resolution schlieren images of three C shocks from different shots at different times are shown in Figs. 3(a)–3(c). The schlieren images show two horizontal shocks encompassing a post-shock region. Initially, as seen in Fig. 2(a), the entire shock structure measures 0.1–0.2 cm ($\sim\lambda_{\text{mfp-ii}}$). Figures 3(a)–3(c) show that they expand in the axial direction at $\leqslant 2\times10^6$ cm/s for 100–200 ns, and remain generally featureless and symmetrical for over 400 ns after formation, beyond which time no data was collected. The varied positions of the different C shocks seen in Figs. 3(a)–3(c) relative to the vertical midplane are likely due to jet asymmetries caused by array defects introduced during loading into GenASIS. Even with these initial asymmetries the shocks are reproducible in size and shape from shot to shot.

While Λ_C at measured densities for C does increase as T_e falls from 30 to ~5 eV, simple calculations of shock jump conditions indicate that the electrons will heat up to ~50–100 eV, and cooling them to $\leqslant$30 eV (where cooling instabilities might begin forming) would take longer than the experimental window. As such, no thermal condensation instabilities are expected in the C shocks.

Copper flows interact to form a post-shock region about 0.1 cm thick [see Fig. 2(c)] that expands slowly (1×10^6–2×10^6 cm/s) over the first ~40 ns of formation, after which time the shock structure grows unpredictable. This unpredictability is demonstrated in the schlieren images in Figs. 3(d)–3(f). Some shocks remain a single unstable shock [Fig. 3(f)] while others fragment into two or more pieces within the first 75 ns of formation, as seen beginning in Fig. 2(d) and resulting in the shock shown in Fig. 3(d) (these images are from the same shot).

Schlieren images of Cu shocks [such as in Figs. 3(d)–3(f)] show density perturbations with wavelengths ranging from ~0.05–0.2 cm. This could be due to the strong cooling of the Cu plasma since calculations show Cu shocks cool significantly in the time span of a few nanoseconds. Any observed perturbations are unlikely to be thermal condensation instabilities though, because in the limited ranges where Λ_C increases with falling temperature, either thermal equilibration dominates (at high temperatures) or the perturbations are too small to resolve ($\leqslant$100 μm at low temperatures). The inconsistency and small size of the Cu shocks and fragments makes analyzing the perturbations and evolution difficult, and as a result the mechanisms driving Cu shock behavior, be they predominantly cooling or collisionality related, remain unknown to the authors.

With a minimum $\lambda_{\text{mfp-ii}} \geqslant 2$ cm, most W ions will typically travel the entire 1.6 cm floating electrode gap without experiencing a collision with an ion from the opposing jet. As mentioned earlier, opposing *e-i* collisions happen slightly more frequently between jets ($\lambda_{\text{mfp-ie}} \sim 0.8$ cm), but probably not enough to significantly alter ion momentum. As a consequence of this, W flows do not form strong perpendicular shocks. They instead develop axial perturbations as seen in the schlieren image in Fig. 4. A brief increase in electron density (greater than the simple doubling of the electron density in overlapping jets) forms when the flows first meet and this fragments in <10–15 ns (the time between XUV or laser probing images). Identifiable features separate at around 5×10^6 cm/s [two have been marked with colored arrows in Figs. 2(e) and 2(f)]. Upon fragmenting, the denser 'seeds' appear to trail axial filaments of higher-density plasma, which exist in some form for at least another 150 ns across the length of the interaction region, as shown in Fig. 4. Whether these correlate to filamentary structures seen in SNRs remains to be determined.

Results presented to this point show a transition from weakly-cooled and collisional C shocks to effectively collisionless W interactions. What intermediate physics

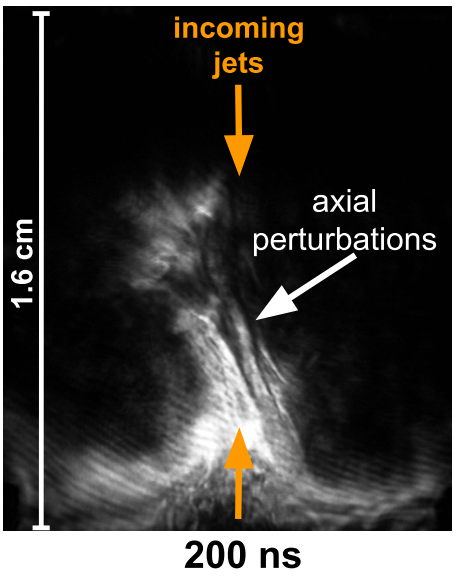

FIG. 4. A schlieren image of a W-W jet shot at 200 ns after initial interaction. The direction of the jets are labeled with orange arrows. A white arrow points to the region where defined axial perturbations formed with transverse wavelengths of 0.06–0.2 cm. The absence of a visible top jet in this figure is likely due to the thin support element holding the schlieren stop in place blocking it.

occurs in the unstable, weakly collisional, and strongly cooled Cu interactions so far remains unclear. Some answers though, may lie in the complex but structurally stable post-shock regions formed by weakly collisional, moderately cooled Al flows.

As shown in Figs. 5(a)–5(c), Al shocks form, grow, and survive comparably to C shocks, but unlike C shocks, the Al postshock region develops substantial small-scale texture within the first 90 ns of evolution that grows in complexity with time. The nature of the perturbations in the Al postshock regions, be they formed by cooling instabilities, turbulence, or some other effects of interpenetration due to the weak collisionality may offer clues as to why the Cu shocks grew unstable so quickly.

The Al cooling function (Λ_c) at measured densities increases with decreasing temperature in the ranges of 200–100 eV, and 10–5 eV. Thermal conductivity from 200–100 eV is too large to facilitate instability growth. However, regardless of the initial shock temperature, the postshock region should cool down quickly (tens of ns) into the 10–5 eV temperature range. At 5 eV, the wavelength of maximum growth is of the order of 0.06 cm. Manual measurements of density 'clumps' seen in gated optical and schlieren images show some in this wavelength. Power spectral density (PSD) plots of fully developed Al shocks such as the 280 ns plot in Fig. 5(d) show a small local maximum at a wave number $k \approx 10^2$ rad/cm, corresponding to $\lambda = 0.06$ cm, which could very well be indicative of the thermal condensation instability.

Despite the quantitative evidence of thermal condensation instabilities, the wide range of wavelengths seen in the Al shock cell perturbations means that these thermal condensation instabilities may contribute to, but not completely explain the structure in the postshock region. In order to test whether the texture in the experimental Al postshock regions approach the $\leqslant k^{-5/3}$ Kolmogorov criterion for a turbulent fluid (or $\sim k^{-2}$ for Burger's turbulence in a compressible fluid), PSD vs wave number (k) plots were created from all schlieren images of Al shocks [33–35]. Though limited in that PSD plots are quite sensitive to initial conditions, they give a fair quantitative picture of the overall structural trends in the postshock regions.

Provided that the three-dimensional (3D) perturbation statistics are isotropic, the k dependence of the

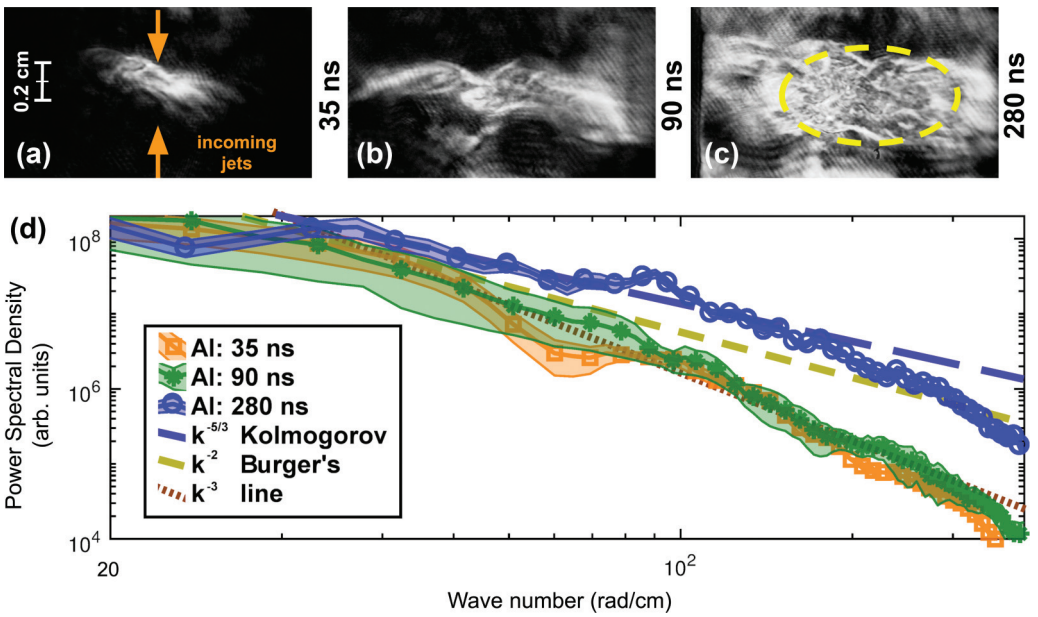

FIG. 5. (a)–(c) Three schlieren images of Al shocks at ~35, 90, and 280 ns after shock formation qualitatively showing the increase in small-scale structure. d) A PSD vs wave number plot of the three Al shocks in (a)–(c) showing the quantitative increase in complex structure over time. Trendlines for Kolmogorov ($k^{-5/3}$) and Burger's ($\sim k^{-2}$) turbulence as well as k^{-3} are provided for reference.

one-dimensional (1D) PSD is proportional to the radially averaged profile taken from the 2D PSD plots. The relationship between the transmitted intensity of light in a schlieren image and density is described in detail in the supplementary materials of White *et al.* (Ref. [36]) and the methods used to produce the power spectra shown in Fig. 5(d) borrow heavily from this work. One key difference between the setup used here and that detailed in White *et al.* is the use of the radial schlieren stop in this work compared to a 1D knife edge in Ref. [36]. A rough spectral comparison of PSD plots from simultaneously acquired spherical and 1D stop schlieren images suggest that they decay within 10–20% of one another, which is adequate to show trends without making definitive claims. A further concern is that generally when declaring the presence of turbulence via power spectra, one wants to observe the PSD decaying at a turbulent rate for multiple orders of magnitude. This is extremely difficult experimentally though, and may not even be possible due to optical resolution limits and a limited range of acceptable wavelengths over which turbulence can occur in this system.

Having acknowledged their limitations, PSD plots of three different Al shocks spanning from ∼35–280 ns after shock formation are shown in Fig. 5(d). The early time (35 and 90 ns) plots show a steep decay in power across all wave numbers, with an average slope of $\sim k^{-3}$. Beyond ∼100 ns, the complexity of the structures increases and this is reflected in the power spectra initially decaying with a much shallower slope. The PSD of the Al shock at 280 ns (blue circles) decays from 0.2 cm to ∼0.03 cm ($k = 30$–200 rad/cm) with a slope between $k^{-5/3}$ and k^{-2}. The shaded error bars in Fig. 5(d) are produced by averaging PSD plots from four regional selections of each shock [the area from which these regions were selected is indicated by the dashed oval in Fig. 5(c)]. The decrease in negative slope of the power spectra with time reflects the visible trend towards increasing small-scale postshock structures, and may be evidence of turbulence developing in the Al postshock regions. What generates such potential turbulence and what role it may play in breaking up the Cu shocks is an area for future study.

V. CONCLUDING REMARKS

Presented here are four distinct interactions of supersonic plasma flows using four different materials in an identical configuration. The results span from simple collisional shocks, to strongly cooled and weakly collisional flows, to strongly interpenetrating flows. Cursory calculations of the dimensionless scaling criteria described in Refs. [7,8] indicate that the C flows, despite their lack of cooling, may scale to certain aspects of HH objects. Al and Cu flows and shocks scale well to the various conditions found in HH objects. W interactions potentially scale to SNRs, and may assist in studying the structures found therein.

The results presented here show collisional to collisionless plasmas, which will require a multi-code (MHD and PIC) modeling approach that will be the topic of a future publication. Determining the amount of advected magnetic field in the jets and characterizing any self-generated fields is another area of interest for future studies. Experiments exploring the formation mechanisms of the observed perturbations and their role in shock evolution are also planned.

ACKNOWLEDGMENTS

This material is based upon work supported by DOE Grant No. DE-SC0014493 and by the Department of Energy, National Nuclear Security Administration under Award No. DE-NA0003842. The work of A.F.A.B. and G.G. was supported by AWE plc., the Engineering and Physical Sciences Research Council (Grants No. EP/M022331/1 and No. EP/N014472/1) and the Science and Technology Facilities Council of the United Kingdom.

[1] G. H. Herbig, The spectra of two nebulous objects near NGC 1999, Astrophys. J. **113**, 697 (1951).
[2] R. D. Schwartz, A shocked cloudlet model for herbig-haro objects, Astrophys. J. **223**, 884 (1978).
[3] K. W. Weiler and R. A. Sramek, Supernovae and supernova remnants, Annu. Rev. Astron. Astrophys. **26**, 295 (1988).
[4] M. L. Bernet, F. Miniati, S. J. Lilly, P. P. Kronbery, and M. Dessuages-Zevadsky, Strong magnetic fields in normal galaxies at high redshift, Nature **454**, 302 (2008).
[5] B. Reipurth and J. Bally, Herbig-haro flows: Probes of early stellar evolution, Annu. Rev. Astron. Astrophys. **39**, 403 (2001).
[6] K. Koyama, R. Petre, E. V. Gotthelf, U. Hwang, M. Matsuura, M. Ozaki, and S. S. Holt, Evidence for shock acceleration of high-energy electrons in the supernova remnant, Nature **378**, 255 (1995).
[7] D. Ryutov, R. P. Drake, J. Kane, E. Liang, B. A. Remington, and W. M. Wood-Vasey, Similarity criteria for the laboratory simulation of supernova hydrodynamics, Astrophys. J. **518**, 821 (1999).
[8] D. D. Ryutov, B. A. Remington, H. F. Robey, and R. P. Drake, Magnetohydrodynamic scaling: From astrophysics to the laboratory, Phys. Plasmas **8**, 1804 (2001).
[9] J. M. Blondin, A. Königl, and B. A. Fryxell, Herbig-haro objects as the heads of radiative jets, Astrophys. J. Lett. **337**, L37 (1989).
[10] E. M. de Gouveia Dal Pino and R. Opher, A possible origin of the h-h objects in stellar outflows, Rev. Mex. Astron. Astrofis. **21**, 477 (1990).
[11] G. B. Field, Thermal instability, Astrophys. J. **142**, 531 (1965).
[12] M. C. Begelman and C. F. McKee, Global effects of thermal conduction on two-phase media, Astrophys. J. **358**, 375 (1990).
[13] E. S. Weibel, Spontaneously Growing Transverse Waves in a Plasma Due to an Anisotropic Velocity Distribution, Phys. Rev. Lett. **2**, 83 (1959).
[14] A. Balogh and R. A. Treumann, *Physics of Collisionless Shocks, Space Plasma Shock Waves* (Springer-Verlag, New York, 2013).
[15] D. D. Ryutov, F. Fiuza, C. M. Huntington, J. S. Ross, and H.-S. Park, Collisional effects in the ion Weibel instability for two

counter-propagating plasma streams, Phys. Plasmas **21**, 032701 (2014).

[16] F. Suzuki-Vidal, S. V. Lebedev, A. Ciardi, L. A. Pickworth, R. Rodriguez, J. M. Gil, G. Espinosa, P. Hartigan, G. F. Swadling, J. Skidmore, G. N. Hall, M. Bennett, S. N. Bland, G. Burdiak, P. de Grouchy, J. Music, L. Suttle, E. Hansen, and A. Frank, Bow shock fragmentation driven by a thermal instability in laboratory astrophysics experiments, Astrophys. J. **815**, 96 (2015).

[17] N. L. Kugland, D. D. Ryutov, P.-Y. Chang, R. P. Drake, G. Fiksel, D. H. Froula, S. H. Glenzer, G. Gregori, M. Grosskopf, M. Koenig, Y. Kuramitsu, C. Kuranz, M. C. Levy, E. Liang, J. Meinecke, F. Miniati, T. Morita, A. Pelka, C. Plechaty, R. Presura, A. Ravasio, B. A. Remington, B. Reville, J. S. Ross, Y. Sakawa, A. Spitkovsky, H. Takabe, and H.-S. Park, Self-organized electromagnetic field structures in laser-produced counter-streaming plasmas, Nat. Phys. **8**, 809 (2012).

[18] C. M. Huntington, F. Fiuza, J. S. Ross, A. B. Zylstra, R. P. Drake, D. H. Froula, G. Gregori, N. L. Kugland, C. C. Kuranz, M. C. Levy, C. K. Li, J. Meinecke, T. Morita, R. Petrasso, C. Plechaty, B. A. Remington, D. D. Ryutov, Y. Sakawa, A. Spitkovsky, H. Takabe, and H. S. Park, Observation of magnetic field generation via the weibel instability in interpenetrating plasma flows, Nat. Phys. **11**, 173 (2015).

[19] J. S. Ross, D. P. Higginson, D. Ryutov, F. Fiuza, R. Hatarik, C. M. Huntington, D. H. Kalantar, A. Link, B. B. Pollock, B. A. Remington, H. G. Rinderknecht, G. F. Swadling, D. P. Turnbull, S. Weber, S. Wilks, D. H. Froula, M. J. Rosenberg, T. Morita, Y. Sakawa, H. Takabe, R. P. Drake, C. Kuranz, G. Gregori, J. Meinecke, M. C. Levy, M. Koenig, A. Spitkovsky, R. D. Petrasso, C. K. Li, H. Sio, B. Lahmann, A. B. Zylstra, and H.-S. Park, Transition from Collisional to Collisionless Regimes in Interpenetrating Plasma Flows on the National Ignition Facility, Phys. Rev. Lett. **118**, 185003 (2017).

[20] S. V. Lebedev, A. Ciardi, D. J. Ampleford, S. N. Bland, S. C. Bott, J. P. Chittenden, G. N. Hall, J. Rapley, C. Jennings, M. Sherlock, A. Frank, and E. G. Blackman, Production of radiatively cooled hypersonic plasma jets and links to astrophysical jets, Plasma Phys. Control. Fusion **47**, B465 (2005).

[21] D. J. Ampleford, Experimental study of plasma jets produced by conical wire array z-pinches, Ph.D. dissertation, Imperial College London, London, UK, 2005.

[22] J. C. Valenzuela, G. W. Collins, T. Zick, J. Narkis, I. Krasheninnikov, and F. N. Beg, Counter-propagating plasma jet collision and shock formation on a compact current driver, High Energy Density Phys. **17**, 140 (2015).

[23] S. C. Bott, D. M. Haas, R. E. Madden, U. Ueda, Y. Eshaq, G. Collins, K. Gunasekera, D. Mariscal, J. Peebles, F. N. Beg, M. Mazarakis, K. Struve, and R. Sharpe, 250 kA compact linear transformer driver for wire array z-pinch loads, Phys. Rev. ST Accel. Beams **14**, 050401 (2011).

[24] H. R. Griem, *Principles of Plasma Spectroscopy*, Cambridge Monographs on Plasma Physics (Cambridge University Press, Cambridge, 1997).

[25] M. Hipp, J. Woisetschlaeger, P. Reiterer, and T. Neger, Digital evaluation of interferograms, Measurement **36**, 53 (2004).

[26] G. Pretzier, A new method for numerical abel-inversion, Z. Naturforsch. **46**, 639 (1991).

[27] H.-K. Chung, M. H. Chen, W. L. Morgan, Yu-Ralchenko, and R. W. Lee, Flychk: Generalized population kinetics and spectral model for rapid spectroscopic analysis for all elements, High Energy Density Phys. **1**, 3 (2005).

[28] S. C. Bott, D. M. Haas, Y. Eshaq, U. Ueda, R. E. Madden, G. W. Collins, and F. N. Beg, Ablation studies of low-number wire arrays at 200 kA using a linear transformer driver, IEEE Trans. Plasma Sci. **38**, 567 (2010).

[29] A. Ciardi, S. V. Lebedev, J. P. Chittenden, and S. N. Bland, Modeling of supersonic jet formation in conical wire array z-pinches, Laser Part. Beams **20**, 255 (2002).

[30] P. W. Rambo and R. J. Procassini, A comparison of kinetic and multifluid simulations of laser-produced colliding plasmas, Phys. Plasmas **2**, 3130 (1995).

[31] Y. P. Zakharov, Comment on "studying astrophysical collisionless shocks with counterstreaming plasmas from high power lasers", High Energy Density Phys. **8**, 329 (2012).

[32] D. D. Ryutov, N. L. Kugland, H.-S. Park, S. M. Pollaine, B. A. Remington, and J. S. Ross, Collisional current drive in two interpenetrating plasma jets, Phys. Plasmas **18**, 104504 (2011).

[33] A. N. Kolmogorov, The local structure of turbulence in incompressible viscous fluid for very large reynolds numbers, Proc. Math. Phys. Sci. **434**, 9 (1991).

[34] J. Bec and K. Khanin, Burgers turbulence, Phys. Rep. **447**, 1 (2007).

[35] S. S. Girimaji and Y. Zhou, Spectrum and energy transfer in steady burgers turbulence, Phys. Lett. A **202**, 279 (1995).

[36] T. G. White, M. T. Oliver, P. Mabey, M. Kühn-Kauffeldt, A. F. A. Bott, L. N. K. Döhl, A. R. Bell, R. Bingham, R. Clarke, J. Foster, G. Giacinti, P. Graham, R. Heathcote, M. Koenig, Y. Kuramitsu, D. Q. Lamba, J. Meinecke, Th. Michel, F. Miniati, M. Notley, B. Reville, D. Ryu, S. Sarkar, Y. Sakawa, M. P. Selwood, J. Squire, R. H. H. Scott, P. Tzeferacos, N. Woolsey, A. A. Schekochihin, and G. Gregori, Supersonic plasma turbulence in the laboratory, Nat. Commun. **10**, 1758 (2019).

Correction: A minor error in an inline equation appearing in the second paragraph of the Introduction has been fixed and the definition for a corresponding term has been added.